Supplementary Information for "Personalising cardiac electrophysiology models from CT and ECG for 3D activation imaging and tissue characterisation"

S1 Data processing

The clinical body surface potentials (BSPs) recorded by the ECGi-vest were processed to comply with the simulated signals. A time shift was applied to the BSP computed at each electrode location, so that the Q-wave began at approximately time zero. Hence, a linear ramp between endpoints was subtracted from each signal to make first and last voltage values equal to 0 (Fig. S1).

S2 Anatomical model generation

Each mesh of the KCL cohort [1] includes tags for different organs, heart regions, and implantable cardioverter-defibrillator (ICD) leads and cans. We accounted for eleven regions – namely ventricles, atria, inner body (including muscles and fat), blood, bones, kidneys, liver, lungs, spleen, stomach, and skin. Each ICD lead or can was assigned to the medium within which they lied. Specifically, we assigned coronary sinus coil, subcutaneous ICD lead, left can, right can and subcutaneous ICD can to

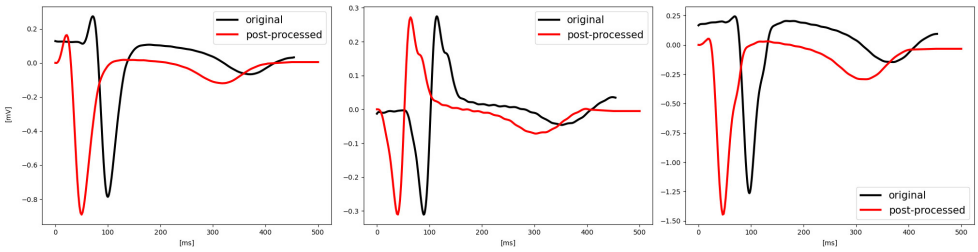

Fig. S1 Pre-processing of clinical body surface potential recordings. Pre-processing of clinical body surface potential recordings. Clinical body surface potentials (BSPs) from the 252-electrode ECGi-vest were pre-processed to align with simulated signals. Three representative electrodes for subject HC1 demonstrate the processing steps. Original recordings (black traces) were time-shifted to align the Q-wave onset to time zero, and a linear ramp was subtracted to ensure initial and final voltage values equal zero (red traces).

the inner body region. Major arteries and veins, cardiac valves, and all blood pools were assigned to the blood region. With respect to the original meshes, we refined the right ventricular (RV) myocardium using the command line tool `meshtool` [2].

We initially segmented anonymised whole torso computed tomography (CT) scans from three healthy volunteers [3] using the open-source tool TotalSegmentator [4] (v1.5.4 for the heart and v2.7.0 for major organs, skin, bones, and vessels) based on nnUNet [5]. We then merged and manually corrected the resulting segmentation classes using Simpleware™ software (Version vX-2025.06; Synopsys, Inc., Sunnyvale, USA). Labels corresponding to the same anatomical group, such as individual bones, were combined. To be consistent with the KCL cohort, we assigned skeletal muscles to the inner body. The cardiac anatomical structures that were automatically segmented include the left ventricular (LV) myocardium and blood pool, the RV, and the left (LA) and right (RA) atria. We generated semi-automatically separate labels for the myocardium and blood pools of LA, RA and RV using Simpleware hollow and logical operator tools. We assigned the septal wall to the LV, justified by the fact that septal depolarisation is mainly driven by the left bundle branch. In addition, we defined four cardiac valves at the junctions of the atria and ventricles, or between the cardiac chambers and major vessels. Each region was refined using the resample

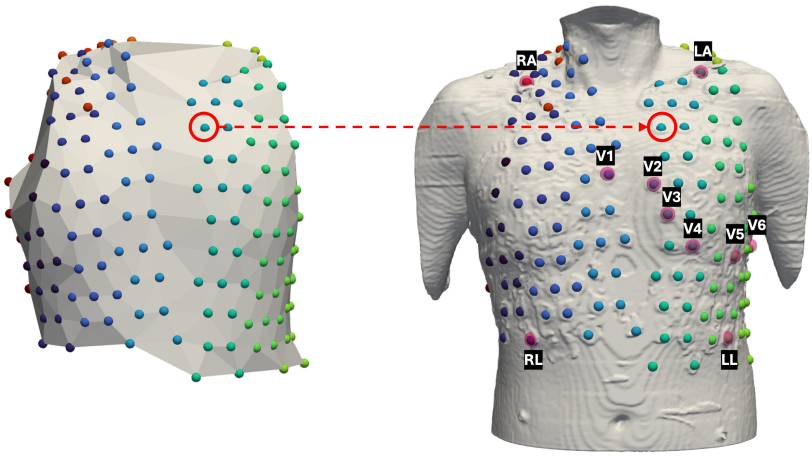

Fig. S2 Mapping of the ECGi-vest onto the anatomical model. The ECGi-vest with 252 electrodes was mapped onto the CT-based mesh using a reference point. The ten electrodes that best correspond to the standard configuration of a 12-lead ECG were manually selected. Different colours refer to different point IDs. The positions of the ten electrodes used to reconstruct the 12-lead ECG is labelled and highlighted in pink. RA = right arm; LA = left arm; RL = right leg; LL = left leg.

algorithm from `meshtool` [2], keeping a conforming interface between the heart and torso. For the HC cohort, we mapped the coordinates of the 252-electrode vest onto the computational mesh as follows. Using ParaView [6], we aligned the torso shell to the CT-based geometry with respect to a selected electrode. Hence, the translated ECGi-vest coordinates were projected on the torso skin (Fig. S2) using a closest point algorithm implemented in Python.

S3 Ion channel densities and variability ranges

In cardiomyocytes, ion channel densities depend on the number of functional channels and are linked to the membrane expression levels of the corresponding channel, pump, or transporter proteins. Information on ion channel expression heterogeneity and variability can be obtained from both protein and mRNA expression data. However, the relationships among mRNA levels, protein abundance, and functional channel conductance are complex and not necessarily linear [7, 8]. Patch-clamp techniques are capable of recording membrane currents, but the number of studies focusing on healthy human

ventricular cardiomyocytes – especially regarding regional differences – is limited [9, 10]. Protein measurement is usually done via Western blotting, which provides only semi-quantitative results. On the other hand, mRNA quantification techniques such as qPCR, microarrays, and RNA sequencing (including single-nucleus RNA sequencing, snRNAseq) are well-established and provide accurate quantification of gene expression.

To estimate variability ranges for the corresponding conductances and model parameters, we used mRNA/gene expression levels of the major ion channel subunits responsible for key membrane currents (Table S1). Relative comparisons (i.e., fold changes) between regions – right and left ventricle, epicardium and endocardium – are used to derived such variability ranges. More specifically,

i We selected three publicly available datasets of gene expression data in healthy human ventricles reported in the literature [11–13]. Each dataset reports quantitative measurements for the selected genes of interest and include samples from distinct ventricular regions.

Observation 1. In [11], high-throughput real-time RT-qPCR (reverse transcription quantitative polymerase chain reaction) was performed on tissue samples from $N = 20$ non-diseased donors (10 female, 10 male) across multiple ventricular regions, namely, right and left ventricle, epi- and endocardium, and for both female and male donors. Data were analysed using the threshold-cycle (C_T) relative-quantification method, with expression levels reported as ratios versus the reference gene HPRT (hypoxanthine-guanine phosphoribosyl transferase) ($2^{-\Delta C_t}$) and summarized as mean ± standard deviation. In [12], analysis of gene expression differences was performed using low-density TaqMan arrays from total RNA extracted from tissue samples of $N = 18$ non-failing hearts (9 female, 9 male). The threshold cycle relative quantification method was applied using GAPDH as an endogenous control. Samples included LV free walls as well as epicardial and endocardial layers. Finally, single-nucleus RNA sequencing (snRNA-seq) data reported in [13] were filtered to retain

only samples from control donors ($N = 15$ for RV, $N = 17$ for septum, $N = 18$ for LV, $N = 12$ for apex). Mean expression values were computed as mean(log1p(counts normalized to 10,000/nucleus)) across all nuclei per donor per region.

ii For each dataset d, the mean μ_X and the standard deviation σ_X of each gene X across samples were computed in each region r. When available, sex was taken into account as an additional category. To keep the notation simple, we denote as X both the gene and the model input associated with it. Hence, the coefficient of variation σ_X/μ_X was used to compute the following scaling factor

$$C_X^{r,d} = e^{1.96\sqrt{\ln(1+(\sigma_X/\mu_X)^2)}} \tag{1}$$

used to translate mRNA data into model parameter ranges.

Observation 2. We assumed that each single-cell model input is a log-normally distributed random variable X with parameters μ_X and σ_X. Hence, $Y := \ln(X) \sim \mathcal{N}(\mu_Y, \sigma_Y)$, with $\mu_Y = \ln(\mu_X^2/\sqrt{\mu_X^2 + \sigma_X^2})$ and $\sigma_Y^2 = \ln(1 + (\sigma_X/\mu_X)^2)$. The 95% confidence interval for the Gaussian variable Y is determined as

$$\mathcal{I}_Y = [\mu_Y - 1.96\sigma_Y, \mu_Y + 1.96\sigma_Y],$$

that is, $\mathbb{P}(y \in \mathcal{I}_Y) \approx 0.95$. Since applying a strictly increasing function to a Gaussian random variable results in a new random variable whose distribution is a monotonic transformation of the original normal distribution, it holds

$$\begin{aligned}
&\mathbb{P}(e^y \in [e^{\mu_Y - 1.96\sigma_Y}, e^{\mu_Y + 1.96\sigma_Y}]) \\
&= \mathbb{P}\left(e^y \in \left[\frac{e^{\mu_Y}}{e^{1.96\sigma_Y}}, e^{\mu_Y} \cdot e^{1.96\sigma_Y}\right]\right)
\end{aligned}$$

$$= \mathbb{P}\left(x \in \left[\frac{\hat{\mu}_X}{e^{1.96\sqrt{\ln(1+(\sigma_X/\mu_X)^2)}}}, \hat{\mu}_X \cdot e^{1.96\sqrt{\ln(1+(\sigma_X/\mu_X)^2)}}\right]\right) \approx 0.95,$$

where $x = e^y$ and $\hat{\mu}_X = e^{\mu_Y}$ is the median of $X = e^Y$. We thus defined the range of variability for each parameter X as

$$\mathcal{I}_X = [X_{baseline}/C_X, X_{baseline} \cdot C_X] \tag{2}$$

where $C_X = e^{1.96\sqrt{\ln(1+(\sigma/\mu)^2)}}$ is the scaling factor and $X_{baseline}$ is the baseline value for the model input.

iii The median scaling factor C_X^d among different regions was then computed, and the maximum value C_X across the datasets was selected. If multiple genes are responsible for the same ionic current, the maximum value was chosen. This gave us a map between genes and model parameters.

iv Finally, the variability range for each model input was defined as

$$\mathcal{I}_X = [X_{baseline}/C_X, X_{baseline} \cdot C_X],$$

where $X_{baseline}$ denotes the corresponding baseline value, as reported in [14].

This allowed us to derive variability ranges based on inter-patient differences in expression levels, rather than on absolute abundance, in the healthy human population.

S3.1 Tissue heterogeneity

Measurements of gene expression profiles taken from different cardiac regions can offer valuable insights into the direction of heterogeneity of the investigated gene and, to some extent, the specific protein it encodes. When the direction of this gradient was

Table S1 Cardiomyocyte genes and proteins. Key genes, encoded proteins and the corresponding ion channel currents or fluxes included in the electrophysiology model. SR = sarcoplasmic reticulum.

Gene	Protein	Cell membrane current/flux and calcium buffer
KCNJ2	Kir2.1	Inward rectified potassium current I_{K1}
KCNJ12	Kir2.2	Inward rectified potassium current I_{K1}
KCNH2	hERG (Kv11.1)	Rapid delayed rectifier potassium current I_{Kr}
KCNQ1	KvLQT1 (Kv7.1)	Slow delayed rectifier potassium current I_{Ks}
KCNE1	minK	Slow delayed rectifier potassium current I_{Ks}
SCN5A	Nav1.5	Sodium current I_{Na}
SCN5A	Nav1.5	Late sodium current I_{NaL}
SLC8A1	NCX1	Sodium-calcium exchange current I_{NCX}
KCND3	Kv4.3	Transient outward potassium current I_{to}
KCNIP2	KChIP2	Transient outward potassium current I_{to}
RyR2	ryanodine receptor 2	Total calcium release via ryanodine receptors from junctional SR
ATP2A2	SERCA2a	Total calcium uptake via SERCA pump to network SR
CACNA1C	Cav1.2	L-type calcium current I_{CaL}
ATP1A1	α1 Na+/K+-ATPase	Sodium-potassium pump current P_{NaK}
ATP1B1	β1 Na+/K+-ATPase	Sodium-potassium pump current P_{NaK}
CALMx (1,2,3)	Calmodulin x (1,2,3)	Total calmodulin concentration in cytoplasm
CASQ2	Calsequestrin 2	Total calsequestrin concentration in junctional SR
TNNC1	Troponin C	Total troponin concentration in cytoplasm

Table S2 Direction of ion channel density gradients. Physiologically-constrained bounds for heterogeneity gradients in the transmural (ρ) and apico-basal (Z) directions of key ion channel conductances. Gradients ≥ 1 indicate that the value at the base or endocardium is greater than or equal to the corresponding value at the apex or epicardium. Only conductances for which at least two independent sources agreed on the gradient direction were included. Ca^{2+} = calcium; Cl^{-} = chloride; K^{+} = potassium; Na^{+} = sodium.

Parameter	Symbol	∇_ρ	∇_Z	References
Conductance of inward K^+ rectifier current	G_{K1}	≤ 1	–	[16, 17]
Conductance of background K^+ current	G_{Kb}	≥ 1	–	[16, 17]
Conductance of rapid delayed K^+ rectifier current	G_{Kr}	≤ 1	–	[16, 18–21]
Conductance of slow delayed K^+rectifier current	G_{Ks}	≤ 1	≤ 1	[16, 17, 22]
Conductance of Na^+-Ca^{2+} exchanger	G_{NCX}	≤ 1	–	[16, 17, 20, 23]
Conductance of transient outward K^+ current	G_{to}	≤ 1	–	[9, 16, 19, 20, 24–26]
Conductance of L-type Ca^{2+} current	P_{Ca}	≤ 1	–	[16, 20, 23, 27]

known – either from gene expression data or organ-level observations – the corresponding variability range was adjusted accordingly (Table S2). For a list of spatial variations in ionic currents underpinning repolarisation heterogeneity found in the literature we refer to [15]. In the case of the apico-basal gradient of the rapid delayed rectifier potassium current, while literature suggests higher hERG gene expression at the base compared to the apex, our numerical simulations resulted in T-wave with discordant polarity with respect to the QRS complex. For this reason, no direction of heterogeneity was imposed.

S4 Testing the reaction-eikonal model with different settings

For a fixed set of parameter values, we compared the QRS complex simulated using i) the reaction-eikonal model with (RE^+) and without (RE^-) diffusion, ii) the RE^- model with the ToR-ORd-dynCl [14] and the ten Tusscher-Panfilov [28] ionic model, and iii) the RE^- model with different time steps Δt, namely 5 and 25 μs. The largest error was observed in the last time steps when using different ionic models (Figure

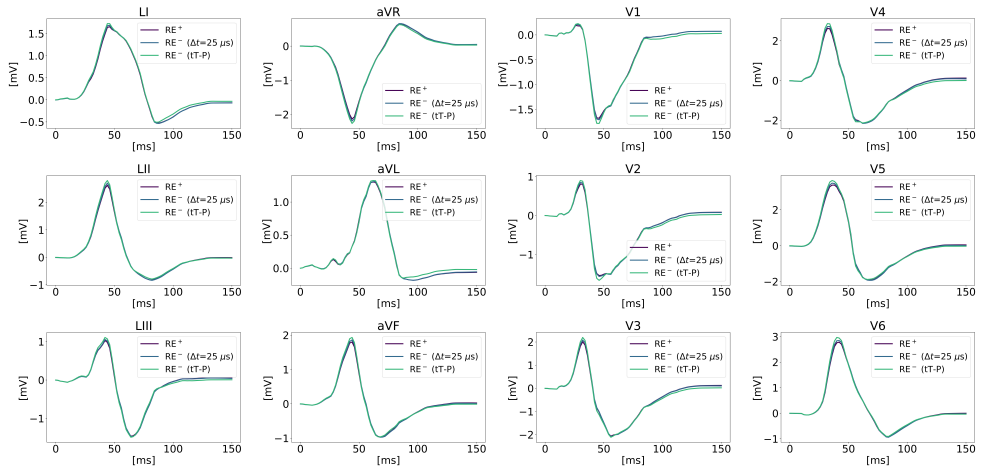

Fig. S3 Simulations of ventricular depolarisation using the reaction-eikonal model. The reaction-eikonal model was coupled with the ToR-ORd-dynCl ionic model with (RE^+, purple) and without (RE^-, Δt=25μs, blue) diffusion, for the same input parameters. The RE^- model was also coupled with the ten Tusscher-Panfilov ionic model (RE^-, tT-P, teal). Simulations were performed for subject KCL1. RE = reaction-eikonal.

Table S3 Computational times of ventricular depolarisation using the reaction-eikonal model. Simulation runtimes across combinations of reaction-eikonal model settings, ionic model choices, and numerical time steps are reported. All simulations were run for a final simulated time of 150 ms using 32 core. Simulations were performed for subject KCL1. RE^+: reaction-eikonal model with diffusion; RE^-: reaction-eikonal model without diffusion.

Model	**Time step** [μs]	**Ionic model**	**Computational time** [s]
RE^+	5	ToR-ORd-dynCl [14]	2220
RE^-	5	ToR-ORd-dynCl [14]	1358
RE^-	25	ToR-ORd-dynCl [14]	154
RE^-	25	ten Tusscher-Panfilov [29]	22

S3). Overall, negligible differences were noticed among the compared solutions. On the other hand, larger discrepancies in computational times were obtained (Table S3).

S5 Sensitivity analysis results

We performed global sensitivity analysis on the ToR-ORd-dynCl model, using emulators to compute Sobol' first-order and the total effects (Fig. S4).

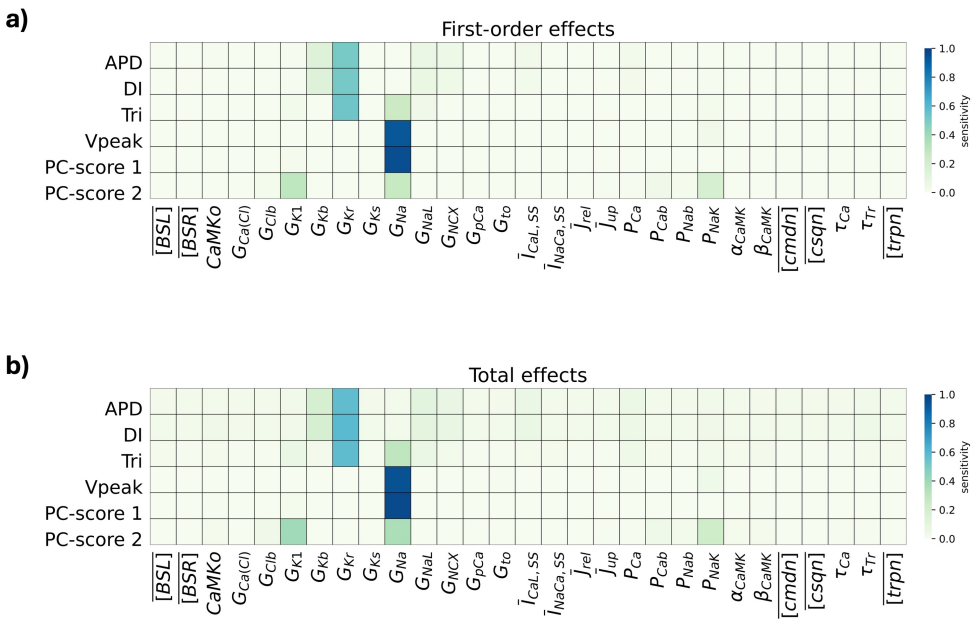

Fig. S4 Parameter sensitivity of action potential morphology. Sobol' **(a)** first-order, and **(b)** total effects quantifies the influence of each ToR-ORd-dynCl model parameter on the action potential morphology. Each subplot shows a heat map of the normalised sensitivity indices of each input (columns) over each output (rows). The darker the cell colour, the larger the influence of an input on that particular output. Outputs are: action potential duration, diastolic interval, triangulation, peak of the action potential, and principal component (PC) scores of upstroke velocity (PC-score 1 and 2). See Table 1 in the Manuscript for parameter definitions. APD = action potential duration; DI = diastolic interval; TRI = triangulation; Vpeak = peak of the action potential; PC = principal component.

For the KLC cohort, the sensitivity indices of the model inputs to the QRS complex and the T-wave morphology are displayed in Fig. S5 and S6, respectively.

S6 Bayesian history matching results

Fig. S7 and S8 show the convergence of the first PC-scores of the QRS complex for the KCL and the HC cohorts, respectively. Similarly, Fig. S9 and S10 show the convergence of the first PC-scores of the T-wave. The total number of waves varied between 5 and 10 among the geometries, with an average of 8 waves. In most cases, the PC-scores predicted in the last HM wave (for the NIMP samples) fell within 3 standard deviations

σ_{PC_q} of their mean μ_{PC_q}. Here, σ_{PC_q} was computed using the outputs extracted from the same ECGs employed to construct the principal component analysis (PCA) bases. Moreover, the mean GPE-prediction fell within 3 standard deviations σ_q of the output μ_q, where $\sigma_q = 0.1\mu_q$.

S7 Model calibration results

Fig. S11 shows the concatenated QRS complexes for the best-fitting signal (smallest root mean squared error) and the synthetic target, for the KCL cohort. These signals were obtained by taking the linear combination of the PCA basis functions with the (predicted/computed) principal component (PC) scores.

The simulated 12-lead ECGs for $N_{val} = 100$ samples are reported in Fig. S12 and S13 for subject HC2 and HC3, respectively. Fig. S14 reports the target and simulated lead II ECGs, used to compute clinical outputs of interest.

S8 Model validation results

Fig. S15 shows different views of the ECGi-vest, with each electrode coloured based on the maximum Pearson's correlation coefficient (PCC), for the HC cohort. The smallest PCCs were computed for electrodes located on the lower right chest and the left lateral-to-central back, consistently across the subjects.

References

[1] Qian S, Bishop M.: Whole Torso Computational Models. Zenodo. Available at Zenodo. Available from: https://doi.org/10.5281/zenodo.7253863.

[2] Neic A, Gsell MAF, Karabelas E, Prassl AJ, Plank G. Automating image-based mesh generation and manipulation tasks in cardiac modeling workflows

using Meshtool. SoftwareX. 2020;11:100454. https://doi.org/10.1016/j.softx.2020.100454.

[3] Isbister JC, Strocchi M, Riedy M, Yeates L, Gray B, Singer ES, et al. Noninvasive assessment of hydroquinidine effect in Brugada syndrome (QUIET BrS). Heart Rhythm. 2024;https://doi.org/10.1016/j.hrthm.2024.12.014.

[4] Wasserthal J, Breit HC, Meyer MT, Pradella M, Hinck D, Sauter AW, et al. TotalSegmentator: Robust Segmentation of 104 Anatomic Structures in CT Images. Radiol Artif Intell. 2023;5(5):e230024. https://doi.org/10.1148/ryai.230024.

[5] Isensee F, Jaeger PF, Kohl SAA, Petersen J, Maier-Hein KH. nnU-Net: a self-configuring method for deep learning-based biomedical image segmentation. Nat Methods. 2021;18(2):203–211. https://doi.org/10.1038/s41592-020-01008-z.

[6] Ayachit U. The ParaView Guide: A Parallel Visualization Application. Kitware; 2015.

[7] Opthof T, Remme CA, Jorge E, Noriega F, Wiegerinck RF, Tasiam A, et al. Cardiac activation–repolarization patterns and ion channel expression mapping in intact isolated normal human hearts. Heart Rhythm. 2017;14(2):265–272. https://doi.org/10.1016/j.hrthm.2016.10.010.

[8] Boyett MR. 'And the beat goes on' The cardiac conduction system: the wiring system of the heart. Exp Physiol. 2009;94(10):1035–1049. https://doi.org/10.1113/expphysiol.2009.046920.

[9] Näbauer M, Beuckelmann DJ, Überfuhr P, Steinbeck G. Regional differences in current density and rate-dependent properties of the transient outward current in subepicardial and subendocardial myocytes of human left ventricle. Circulation.

1996;93(1):168–177. https://doi.org/10.1161/01.cir.93.1.168.

[10] Coppini R, Ferrantini C, Yao L, Fan P, Del Lungo M, Stillitano F, et al. Late Sodium Current Inhibition Reverses Electromechanical Dysfunction in Human Hypertrophic Cardiomyopathy. Circulation. 2013;127(5):575–584. https://doi.org/10.1161/CIRCULATIONAHA.112.134932.

[11] Gaborit N, Varro A, Le Bouter S, Szuts V, Escande D, Nattel S, et al. Gender-related differences in ion-channel and transporter subunit expression in non-diseased human hearts. J Mol Cell Cardiol. 2010;49(4):639–646. https://doi.org/10.1016/j.yjmcc.2010.06.005.

[12] Ambrosi CM, Yamada KA, Nerbonne JM, Efimov IR. Gender Differences in Electrophysiological Gene Expression in Failing and Non-Failing Human Hearts. PLoS One. 2013;8(1):e54635. https://doi.org/10.1371/journal.pone.0054635.

[13] Reichart D, Lindberg EL, Maatz H, Miranda AM, Viveiros A, Shvetsov N, et al. Pathogenic variants damage cell composition and single cell transcription in cardiomyopathies. Science. 2022;377(6606):eabo1984. https://doi.org/10.1126/science.abo1984.

[14] Tomek J, Bueno-Orovio A, Rodriguez B. ToR-ORd-dynCl: an update of the ToR-ORd model of human ventricular cardiomyocyte with dynamic intracellular chloride. bioRxiv. 2020;https://doi.org/10.1101/2020.06.01.127043.

[15] Camps J, Wang ZJ, Doste R, Berg LA, Holmes M, Lawson B, et al. Harnessing 12-lead ECG and MRI data to personalise repolarisation profiles in cardiac digital twin models for enhanced virtual drug testing. Med Image Anal. 2025;100:103361. https://doi.org/10.1016/j.media.2024.103361.

[16] O'Hara T, Virág L, Varró A, Rudy Y. Simulation of the undiseased human cardiac ventricular action potential: model formulation and experimental validation. PLoS Comput Biol. 2011;7(5):e1002061. https://doi.org/10.1371/journal.pcbi.1002061.

[17] Bartolucci C, Passini E, Hyttinen J, Paci M, Severi S. Simulation of the Effects of Extracellular Calcium Changes Leads to a Novel Computational Model of Human Ventricular Action Potential With a Revised Calcium Handling. Front Physiol. 2020;11:314. https://doi.org/10.3389/fphys.2020.00314.

[18] Szabó G, Szentandrássy N, Bíró T, Tóth BI, Czifra G, Magyar J, et al. Asymmetrical distribution of ion channels in canine and human left-ventricular wall: epicardium versus midmyocardium. Pflugers Arch. 2005;450(5):307–316. https://doi.org/10.1007/s00424-005-1445-z.

[19] Szentandrássy N, Bányász T, Bíró T, Szabó G, Tóth BI, Magyar J, et al. Apico-basal inhomogeneity in distribution of ion channels in canine and human ventricular myocardium. Cardiovasc Res. 2005;65(4):851–860. https://doi.org/10.1016/j.cardiores.2004.11.022.

[20] Bartos DC, Grandi E, Ripplinger CM. Ion Channels in the Heart. Compr Physiol. 2015;5(3):1423–1464. https://doi.org/10.1002/cphy.c140069.

[21] Grandi E, Sanguinetti MC, Bartos DC, Bers DM, Chen-Izu Y, Chiamvimonvat N, et al. Potassium channels in the heart: structure, function and regulation. J Physiol. 2017;595(7):2209–2228. https://doi.org/10.1113/JP272864.

[22] Keller DUJ, Weber FM, Seemann G, Dössel O. Ranking the Influence of Tissue Conductivities on Forward-Calculated ECGs. IEEE Trans Biomed Eng. 2010;57(7):1568–1576. https://doi.org/10.1109/TBME.2010.2046485.

[23] Papp R, Bett GCL, Lis A, Rasmusson RL, Baczkó I, Varró A, et al. Genomic upregulation of cardiac Cav1.2α and NCX1 by estrogen in women. Biol Sex Differ. 2017;8(1):26. https://doi.org/10.1186/s13293-017-0148-4.

[24] Schram G, Pourrier M, Melnyk P, Nattel S. Differential distribution of cardiac ion channel expression as a basis for regional specialization in electrical function. Circ Res. 2002;90(9):939–950. https://doi.org/10.1161/01.res.0000018627.89528.6f.

[25] Nerbonne JM, Kass RS. Molecular physiology of cardiac repolarization. Physiol Rev. 2005;85(4):1205–1253. https://doi.org/10.1152/physrev.00002.2005.

[26] Boukens BJD, Christoffels VM, Coronel R, Moorman AFM. Developmental basis for electrophysiological heterogeneity in the ventricular and outflow tract myocardium as a substrate for life-threatening ventricular arrhythmias. Circ Res. 2009;104(1):19–31. https://doi.org/10.1161/CIRCRESAHA.108.188698.

[27] Fülöp L, Bányász T, Magyar J, Szentandrássy N, Varró A, Nánási PP. Reopening of L-type calcium channels in human ventricular myocytes during applied epicardial action potentials. Acta Physiol Scand. 2004;180(1):39–47. https://doi.org/10.1046/j.0001-6772.2003.01223.x.

[28] ten Tusscher KHWJ, Noble D, Noble PJ, Panfilov AV. A model for human ventricular tissue. Am J Physiol Heart Circ Physiol. 2004;286(4):H1573–H1589. https://doi.org/10.1152/ajpheart.00794.2003.

[29] ten Tusscher KHWJ, Panfilov AV. Modelling of the ventricular conduction system. Prog Biophys Mol Biol. 2008;96(1):152–170. https://doi.org/10.1016/j.pbiomolbio.2007.07.026.

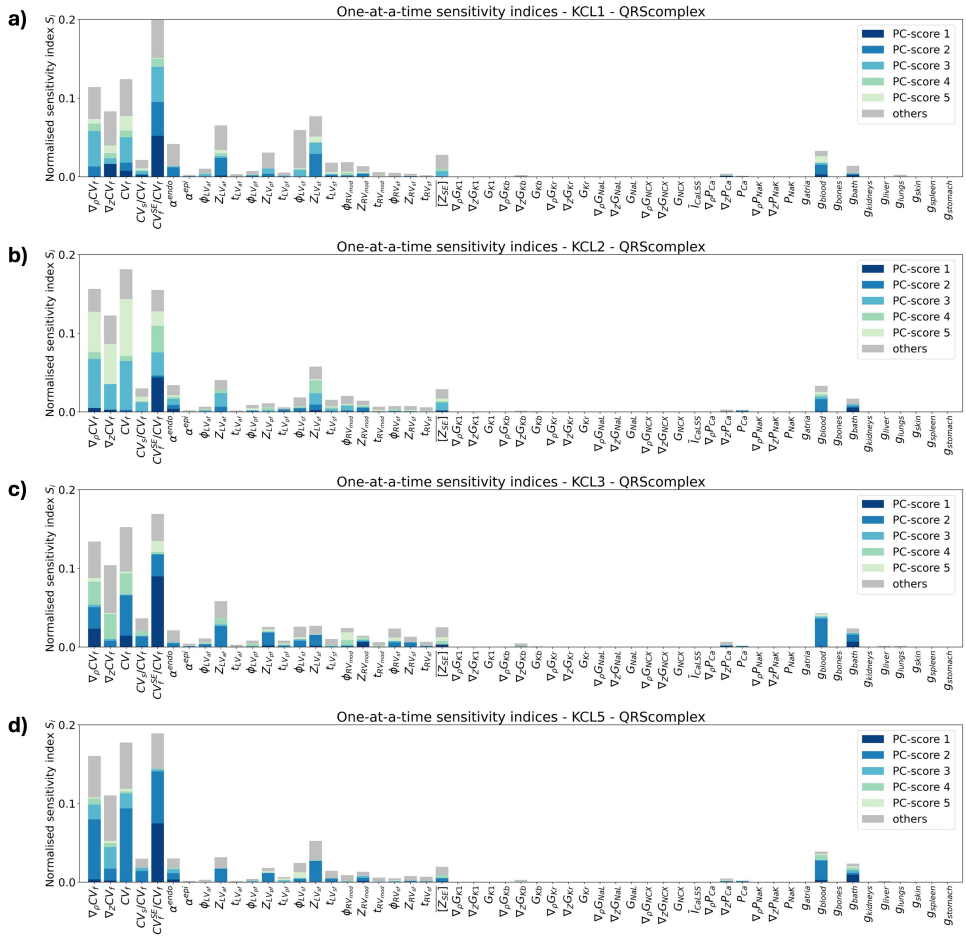

Fig. S5 Parameter sensitivity of QRS complex morphology in the KCL cohort. One-at-a-time sensitivity analysis quantifies the influence of each model parameter on the QRS complex morphology for subjects **(a)** KCL1, **(b)** KCL2, **(c)** KCL3, and **(d)** KCL5. Each subplot shows normalised sensitivity indices (y-axis) for individual parameters (x-axis), with stacked bars representing contributions to different principal component (PC) scores. Bar colours indicate PC-score 1 (dark blue), PC-score 2 (medium blue), PC-score 3 (cyan), PC-score 4 (light cyan), PC-score 5 (pale cyan), and remaining PC-scores (grey). Total bar height represents the cumulative sensitivity index across all PC-scores, providing an overall measure of parameter importance. Parameters are ordered identically across subjects to facilitate comparison. See Tables 1 and 3 in the Manuscript for parameter definitions. PC = principal component.

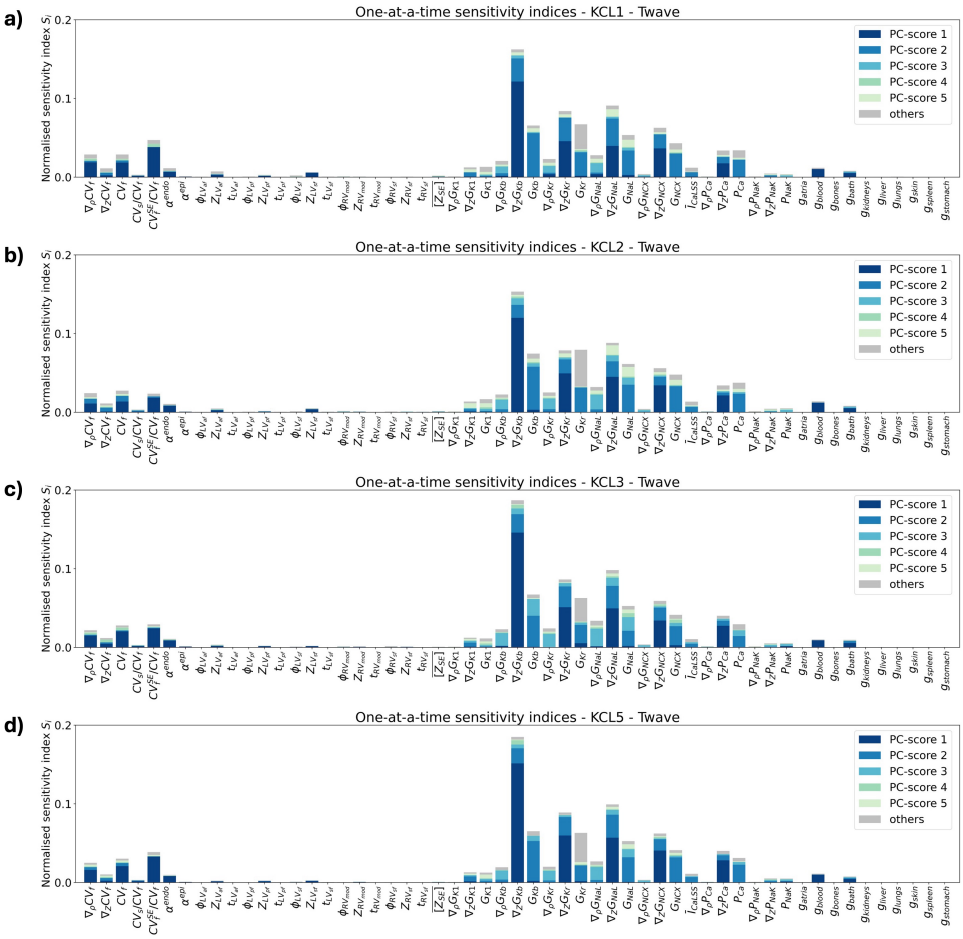

Fig. S6 Parameter sensitivity of T-wave morphology in the KCL cohort. One-at-a-time sensitivity analysis quantifies the influence of each model parameter on the T-wave morphology for subjects **(a)** KCL1, **(b)** KCL2, **(c)** KCL3, and **(d)** KCL5. Each subplot shows normalised sensitivity indices (y-axis) for individual parameters (x-axis), with stacked bars representing contributions to different principal component (PC) scores. Bar colours indicate PC-score 1 (dark blue), PC-score 2 (medium blue), PC-score 3 (cyan), PC-score 4 (light cyan), PC-score 5 (pale cyan), and remaining PC-scores (grey). Total bar height represents the cumulative sensitivity index across all PC-scores, providing an overall measure of parameter importance. Parameters are ordered identically across subjects to facilitate comparison. See Tables 1 and 3 in the Manuscript for parameter definitions. PC = principal component.

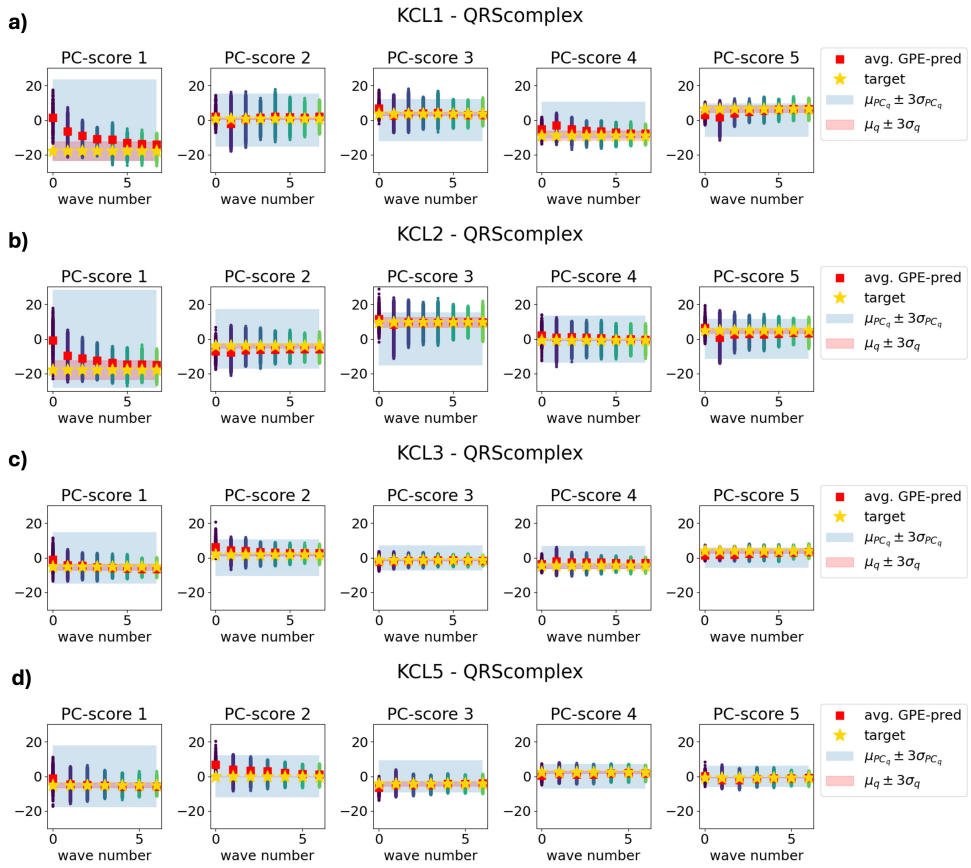

Fig. S7 Convergence of QRS complex PC-scores for the KCL cohort. Each plot shows the Gaussian process emulator (GPE) prediction (y-axis) for 100,000 non-implausible points of each wave (x-axis), sorted in increasing order. Wave 0 corresponds to the initial parameter space. The GPE-prediction mean (red square) and the target principal component (PC)-score (yellow star) are also shown. The red band corresponds to 3 standard deviations (σ_q) from the target output (μ_q). The blue band corresponds to the mean PC-score (μ_{PC_q}) $\pm$ 3 standard deviations (σ_{PC_q}), computed over the samples used to build the principal component analysis basis. GPE = Gaussian process emulator; PC = principal component.

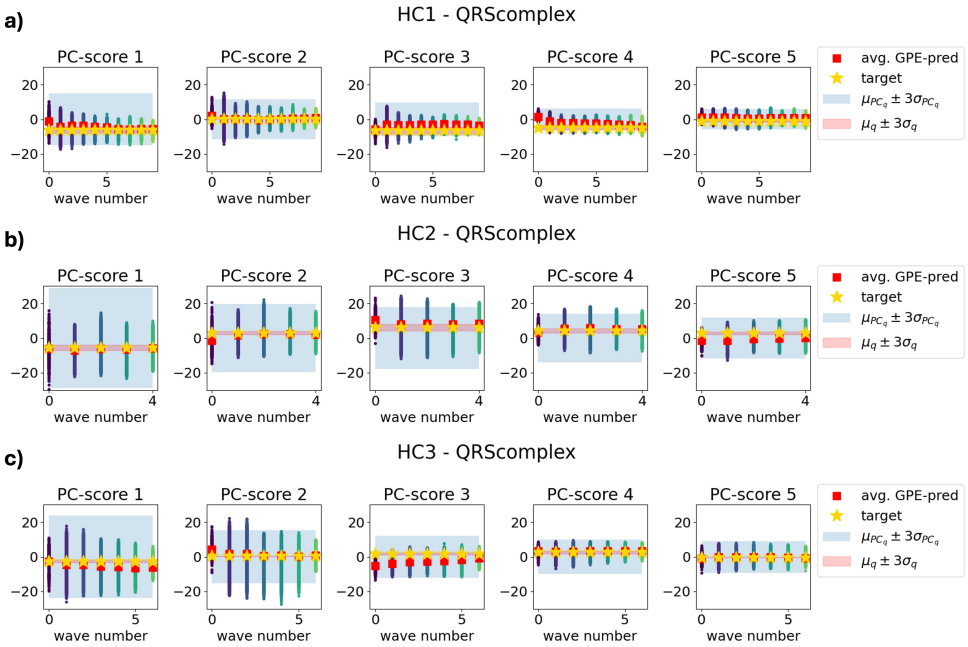

Fig. S8 Convergence of QRS complex PC-scores for the HC cohort. Each plot shows the Gaussian process emulator (GPE) prediction (y-axis) for 100,000 non-implausible points of each wave (x-axis), sorted in increasing order. Wave 0 corresponds to the initial parameter space. The GPE-prediction mean (red square) and the target principal component (PC)-score (yellow star) are also shown. The red band corresponds to 3 standard deviations (σ_q) from the target output (μ_q). The blue band corresponds to the mean PC-score (μ_{PC_q}) $\pm$ 3 standard deviations (σ_{PC_q}), computed over the samples used to build the principal component analysis basis. GPE = Gaussian process emulator; PC = principal component.

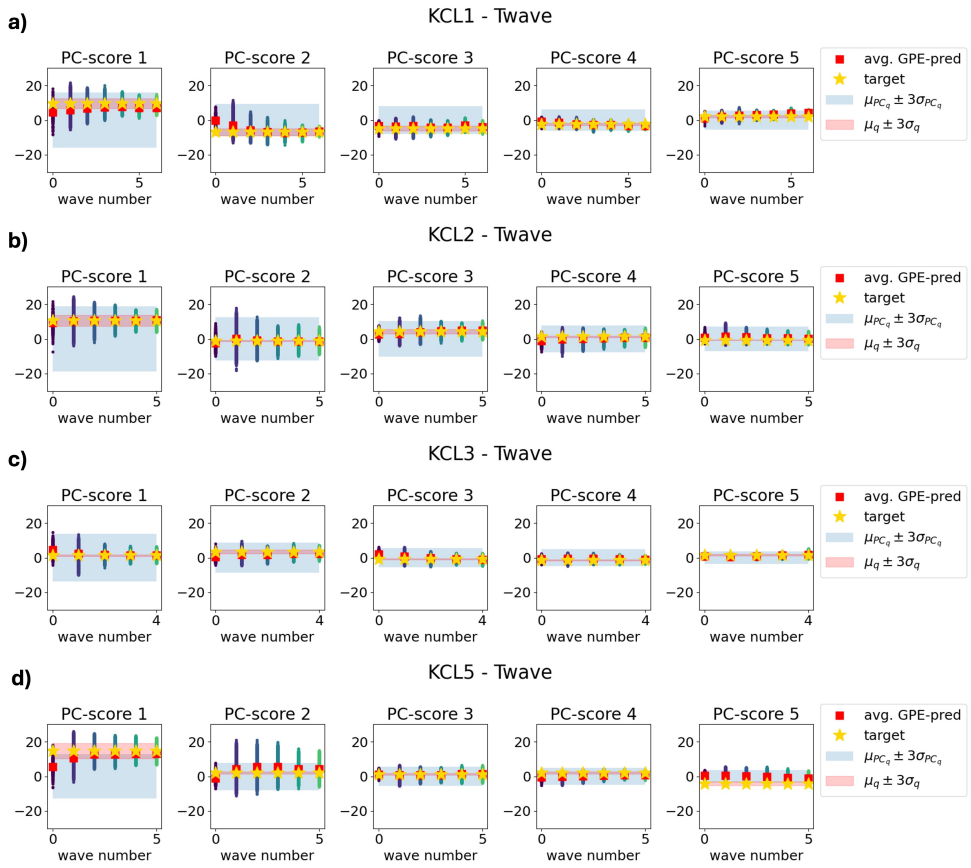

Fig. S9 Convergence of T-wave PC-scores for the KCL cohort. Each plot shows the Gaussian process emulator (GPE) prediction (y-axis) for 100,000 non-implausible points of each wave (x-axis), sorted in increasing order. Wave 0 corresponds to the initial parameter space. The GPE-prediction mean (red square) and the target principal component (PC)-score (yellow star) are also shown. The red band corresponds to 3 standard deviations (σ_q) from the target output (μ_q). The blue band corresponds to the mean PC-score (μ_{PC_q}) $\pm$ 3 standard deviations (σ_{PC_q}), computed over the samples used to build the principal component analysis basis. GPE = Gaussian process emulator; PC = principal component.

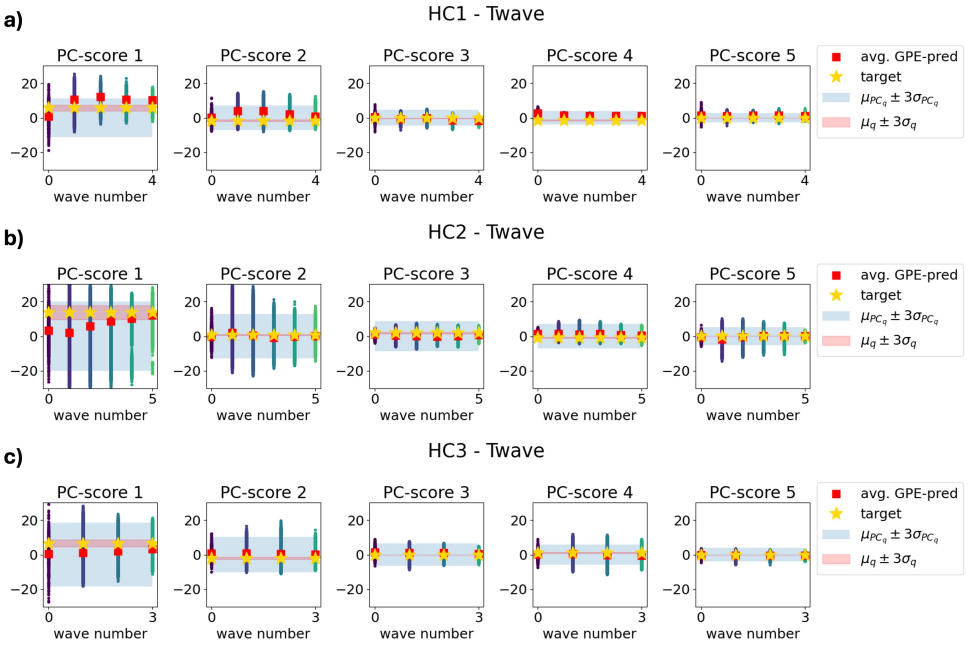

Fig. S10 Convergence of T-wave PC-scores for the HC cohort. Each plot shows the Gaussian process emulator (GPE) prediction (y-axis) for 100,000 non-implausible points of each wave (x-axis), sorted in increasing order. Wave 0 corresponds to the initial parameter space. The GPE-prediction mean (red square) and the target principal component (PC)-score (yellow star) are also shown. The red band corresponds to 3 standard deviations (σ_q) from the target output (μ_q). The blue band corresponds to the mean PC-score (μ_{PC_q}) $\pm$ 3 standard deviations (σ_{PC_q}), computed over the samples used to build the principal component analysis basis. GPE = Gaussian process emulator; PC = principal component.

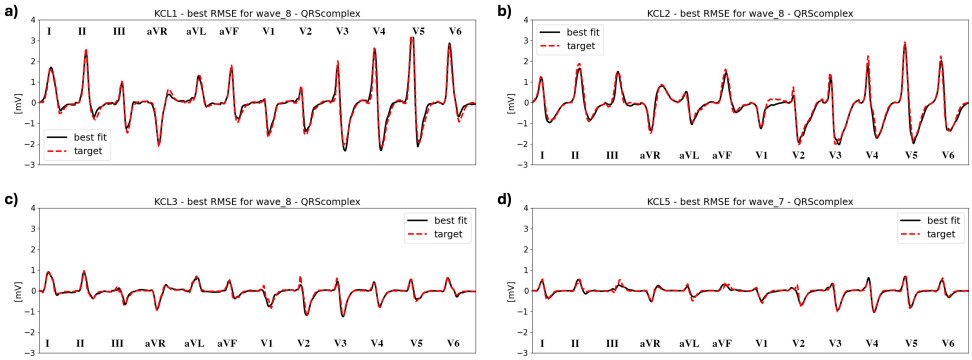

Fig. S11 Model-predicted versus measured QRS complex. Calibrated models accurately reproduce the QRS complex morphology of synthetic 12-lead ECGs for **(a)** KCL1, **(b)** KCL2, **(c)** KCL3, and **(d)** KCL5. Each panel displays QRS complexes arranged in standard clinical order I, II, III, aVR, aVL, aVF and $V1{-}V6$. The dashed red line shows the synthetic target recording. The solid black line shows the best-fitting predicted signal (smallest root mean squared error) from the final wave of Bayesian history matching. Predicted signals were reconstructed as a linear combination of principal component analysis basis functions and principal component scores predicted using Gaussian process emulators.

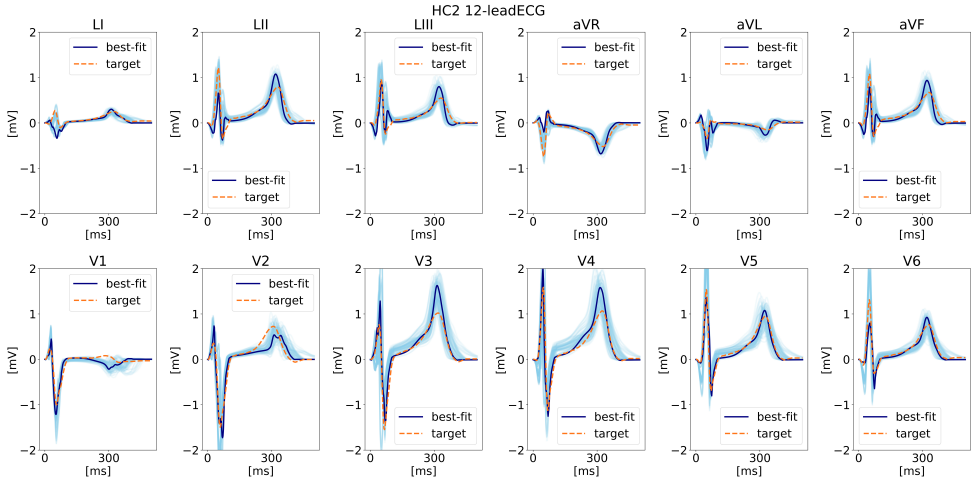

Fig. S12 Simulated 12-lead ECG ensemble for healthy control subject HC2. Validation of the calibrated electrophysiology model for subject HC2 demonstrates robust ECG reproduction across the non-implausible parameter space. Each subplot displays one lead of the 12-lead ECG. Light blue traces represent simulated ECGs from $N_{val} = 100$ validation samples drawn from the final constrained parameter space. The dark blue trace indicates the best-fitting sample (smallest root mean squared error), and the orange dashed trace shows the clinical target recording.

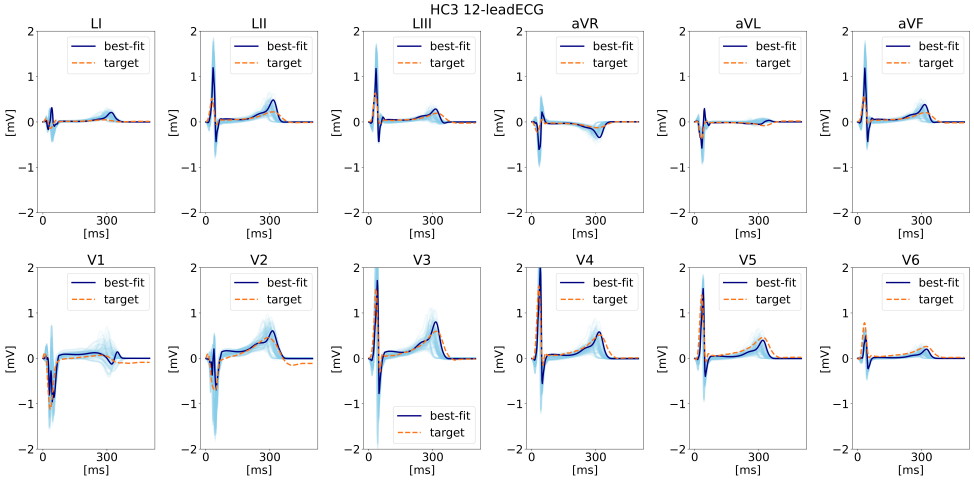

Fig. S13 Simulated 12-lead ECG ensemble for healthy control subject HC3. Validation of the calibrated electrophysiology model for subject HC3 demonstrates robust ECG reproduction across the non-implausible parameter space. Each subplot displays one lead of the 12-lead ECG. Light blue traces represent simulated ECGs from $N_{val} = 100$ validation samples drawn from the final constrained parameter space. The dark blue trace indicates the best-fitting sample (smallest root mean squared error), and the orange dashed trace shows the clinical target recording.

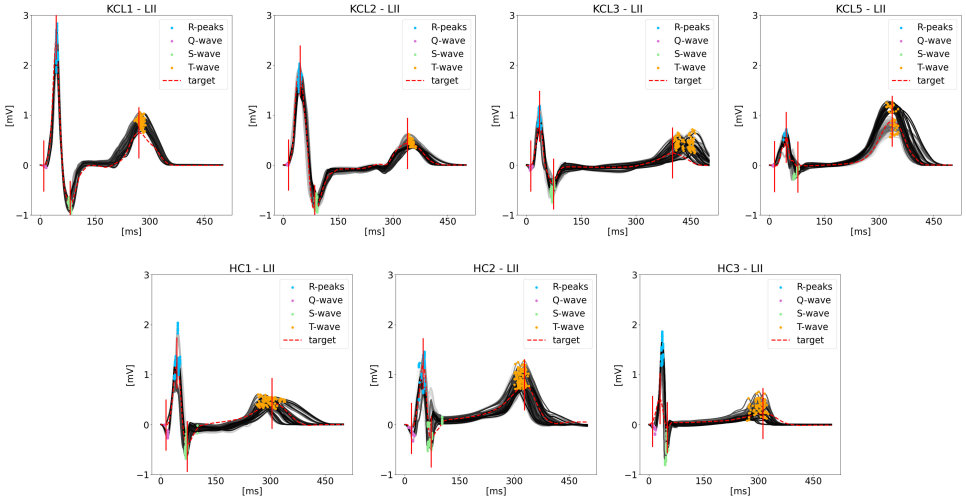

Fig. S14 Lead *II* traces and clinical ECG biomarkers. Lead *II* ECG traces computed for $N_{val} = 100$ validation samples for different subjects. The target signal (red dashed) is also shown. Simulated traces are shown in shades of black. Dots of different colours represent the peaks of the Q (pink), R (blue), S (green), and T (yellow) waves. Red vertical segments highlight the location of the target peaks.

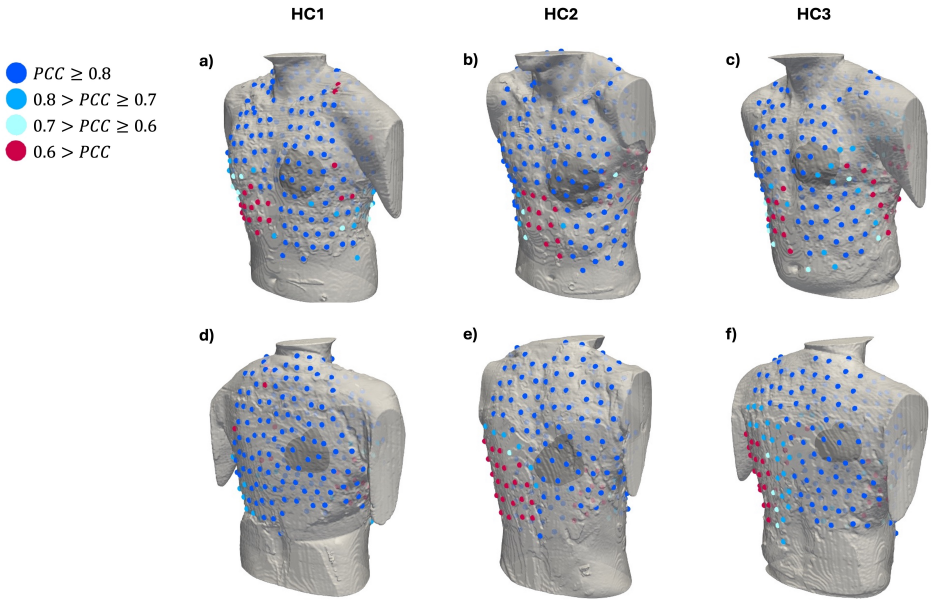

Fig. S15 Spatial distribution of model-measurement correlation for body surface potentials. Spatial patterns of model accuracy are visualised by mapping the maximum Pearson's correlation coefficient (PCC) between simulated and recorded body surface potentials onto the ECGi-vest electrode locations for controls **(a, d)** HC1, **(b, e)** HC2, and **(c, f)** HC3. Anterior **(a–c)** and posterior **(d–f)** views of the torsos are shown. Each electrode is coloured by maximum Pearson's correlation coefficient (PCC) computed across the $N_{val} = 100$ validation simulations (dark blue for $PCC \geq 0.8$, light blue for $0.8 > PCC \geq 0.7$, cyan for $0.7 > PCC \geq 0.6$ and red for $0.6 > PCC$). PCC = Pearson's correlation coefficient.